

Investigation of TESPEL cloud dynamics in Wendelstein 7-X stellarator

G. Kocsis¹, N. Tamura^{2,3}, R. Bussiahn⁴, K.J. McCarthy⁵, J. Baldzuhn⁴, C. Biedermann⁴, G. Cseh¹, H. Damm⁴, P.Kornejew⁴, R. König⁴, N. Panadero⁵, T. Szepesi¹ and the W7-X Team*

¹ Centre for Energy Research, Budapest, Hungary

² National Institute for Fusion Science, National Institutes of Natural Sciences, Toki, Japan

³ The Graduate University for Advanced Studies, SOKENDAI, Toki, Japan

⁴ Max Planck Institute for Plasma Physics, Greifswald, Germany

⁵ Laboratorio Nacional de Fusion, CIEMAT, Madrid, Spain

* author list in T. Klinger et al., 2019 Nucl. Fusion 59 112004

E-mail: kocsis.gabor@energia.mta.hu

Abstract

Tracer-Encapsulated Solid Pellet (TESPEL) was injected from the outboard midplane into Wendelstein 7-X (W7-X) plasmas. Viewing from behind the flight path, the distribution of the light emissions from the TESPEL cloud particles (H, C and C²⁺) was recorded using an ultrafast visible camera with a temporal resolution up to 2 μ s, which allows resolving both the pellet cloud evolution and the detachment of the drifting cloud. It was observed that both the B \perp and the B \parallel aligned dimensions of the pellet cloud fluctuate quasi-periodically, this being associated with a vertical cloud movement and an eruption/ejection of part of the cloud. It is found that, first, the pellet cloud expands parallel to the magnetic field lines for about 10 μ s. Then, when the cloud reaches a certain B \parallel size the ionized part of the cloud (plasmoid) moves vertically (typically upwards) and detaches itself from the pellet within 10 μ s. One possible explanation for the upward movement of the pellet cloud is the presence of a vertical component of grad(B) pointing downward resulting in an upward cloud drift.

Keywords: pellet cloud drift, TESPEL, Wendelstein 7-X

1. Introduction

Cryogenic pellet injection is one of the prime candidates to fuel tokamaks and stellarators [1,2,3]. Pellets are usually injected from the magnetic high-field side (HFS) of axial symmetric tokamaks since in this geometry the grad(B) caused ExB drift pushes the pellet cloud towards the plasma centre [4]. This is favorable for deep particle deposition and higher fueling efficiency [5]. As a contrast, in stellarators the advantage of the HFS pellet injection is not confirmed [3]. The reason for such behavior is not yet understood; it may be a consequence of the complex, three-dimensional magnetic field or the lower magnetic field gradient. Alternatively, cryogenic pellet injection can also play a key role in mitigating Edge Localized Modes (often referred as ELM pacemaking [6,7]) and disruptions (using shattered pellets [8]) in high-confinement tokamak plasmas.

Room temperature solid state pellets (often called impurity pellets) are also injected into magnetically confined plasmas, mainly for diagnostic purposes [9,10]. Their advantages are variable pellet size, starting from the micrometer range, a wide range of selectable materials and the available technologies to manufacture sub-millimeter sized composite pellets [11, 12, 13].

The interaction of pellets and hot plasma is a complex phenomenon, which is not yet fully understood. Nevertheless, the basic processes playing a role are identified and they appear to be similar for both cryogenic and impurity pellets [14,15,16].

When a solid pellet enters the confined plasma, the energy carried by the hot target plasma particles (mainly the electrons) sublimates, and later ablates, the pellet material, forming a dense, neutral and spherically expanding cloud around the pellet. The density, and therefore the shielding properties, of this cloud depends on the sublimation energy of the pellet material. For cryogenic pellets, where the sublimation energy is low, this results in an almost complete shielding [17], while for impurity pellets the shielding factor and therefore the ablation rate depend on the pellet material and size [16]. The spherical expansion

of the pellet cloud turns into a channel flow along the magnetic field lines after the cloud material is ionized, forming a field-line-elongated cloud filament (often called “plasmoid”). Simulations reveal that the length of this plasmoid can be tens of meters, and its pressure is orders of magnitude higher than the target plasma pressure close to the pellet surface, and ten times higher several meters away [18].

In a homogeneous magnetic field, the pellet cloud moves together with the pellet across the magnetic field due to an ExB drift in the self-consistent electric fields [19]. In the case of an inhomogeneous magnetic field, the magnetic field gradient also causes the polarization of the plasmoid which leads (through ExB drift) to the above mentioned drift towards the low-field side (LFS) in tokamaks. If the polarization is not fully compensated for by parallel currents or by Alfvén wave generation, the pellet cloud detaches from the pellet, around which a new cloud is formed.

Pellet cloud drifting was observed in cryogenic pellet injection experiments almost twenty years ago [20]. In the ASDEX Upgrade tokamak, an additional upward movement of the detaching pellet cloud was also observed [21]. The LFS drift was accompanied by fluctuations of the light emitted by pellet cloud particles, which produced a striated emission pattern on long-exposure visible images (“striations”) [22]. Similar fluctuations and striations were also seen in impurity pellet experiments, independently of the pellet material and size [11].

The polystyrene sphere of the Tracer-Encapsulated Solid Pellet (TESPEL) [23] has also low sublimation energy and therefore similar ablation characteristics to those of cryogenic hydrogen (H/D) pellets [24], which makes it suitable and useful for pellet cloud evolution and drift investigations. Moreover, the low order ionic states of carbon (C) can be easily distinguished by spectroscopic methods, allowing us to study both the neutral and the ionized parts of the pellet cloud. The measured radiation (Balmer beta and Bremsstrahlung) distribution of the TESPEL cloud was previously used on the heliotron Large Helical Device (LHD) to determine its electron density and temperature distribution. However, the temporal resolution of this investigation was not enough to resolve the fast processes of the cloud ablation and drift [25,26].

Since pellet ablation and drift processes are known to play a crucial role e.g. for the plasma fueling better understanding of these processes is required to improve plasma performance predictions for next generation fusion reactors [39,40]. With this goal in mind the temporal evolution of the cloud of ablating TESPELs is investigated using spectroscopic methods on the stellarator Wendelstein 7-X (W7-X) and the results are presented in this paper. The distribution of the light emission emitted by the TESPEL cloud particles (Hydrogen, Carbon) was recorded by an ultrafast visible camera with a temporal resolution up to 2 μ s. To our knowledge this is the first experiment which could resolve both the pellet cloud evolution and detachment, and this paper summarizes the obtained results.

2. Experimental setup

W7-X is a medium-sized (major radius 5.5 m, average minor radius 0.53 m, plasma volume ca. 30 m³) superconducting stellarator with 2.5 T magnetic field strength, and has a fivefold symmetry [27, 28]. Its magnetic field was designed to minimize neoclassical transport losses. Accordingly, the rotational transform of the standard configuration is close to unity with a low magnetic shear. By scanning the principal designed magnetic configurations the rotational transform changes from 0.8 to 1.2.

W7-X operation was started at the end of 2015 with a limiter configuration (OP1.1) [29, 30], which was followed by an inertially cooled island divertor campaign (OP1.2). The experiments presented here were conducted in OP1.2, where the available electron cyclotron resonance heating was 7.5 MW and the longest discharge reached 100 s. A comprehensive summary of main results achieved in OP1.2 can be found in [31, 32].

A TESPEL injector, based on the TESPEL injection system developed for LHD [33], was recently installed and commissioned at the AEE41 port of W7-X to support transport investigations [34]. Figure 1 shows the TESPEL injector and the diagnostics whose results are used in this paper. The injector consists of a motorized storage disk with 60 chambers for TESPELs and a gas gun for pellet acceleration. To reduce the propellant gas amount reaching the W7-X vacuum vessel, three expansion chambers were installed along the straight injection line. For a typical pressure of 35 bars of Helium propellant gas, the pellets are accelerated to a velocity in the range of 300-500 m/s and injected radially from the torus outboard. Given that the preparation for TESPEL acceleration takes longer than the current discharge durations, only one TESPEL could be injected per discharge.

The tracer impurity (typically a high-Z material such as iron or tungsten) for impurity transport investigations is embedded into a polystyrene-polymer (C₈H₈)_n spherical shell with an outer diameter of 700 or 900 μ m.

The TESPEL injector is equipped with two light barriers separated by about 110 mm to measure the pellet velocity. A beam splitter cube was installed onto an observation vacuum window (located below the TESPEL entrance port) enabling viewing “from behind”, *i.e.*, along the TESPEL injection line for two diagnostic systems. The light reaching the vacuum window is 50-50% divided between a commercial C-mount lens attached to a 4.5-m-long wound fiber bundle (500x700 individual 10 μ m glass fibers) and a collimating lens focusing the light into an optical fiber. This fiber transfers the captured light from the torus hall to the diagnostic hall where it is fed into a filterscope equipped with seven narrow bandpass interference filters and photomultipliers [34]. The filterscope system records the spectral emission light intensities of the selected tracer elements, as well as carbon and hydrogen (from the polystyrene-polymer shell), with a sampling rate of 2 MHz.

The rear end of the wound fiber is imaged onto the sensor (1024x1024 pixels, 20 μ m pixel size) of a fast framing camera (Photron SA5) by two facing F-mount lenses. By selecting an appropriate focal length ratio ($f = 50$ mm, F1.2 and $f = 85$ mm, F1.4 on the camera) the whole wound fiber bundle covers 425x595 pixels on the sensor. With careful Region of Interest (ROI) selection on the detector chip the temporal resolution of the system could be enhanced up to 2 μ s (525 kHz frame rate @ 64x72 pixels). Wavelength selection interference filters were installed in between the two camera lenses so the incident angle of the rays is close to parallel since the focus of the lenses was set close to infinity. In the study presented here, three different filters were used to separate selected excited ionic species: 538 nm (FWHM: \sim 2.5 nm), 465 nm (FWHM: \sim 2 nm) and 656 nm (FWHM: \sim 3 nm) for C, C²⁺ and H, respectively. Due to the wavelength width of the H α filter some C⁺ radiation may interfere. Figure 2 shows the transmission curves of these filters together with the spectral lines of the above species, which may play an important role in the detected radiation pattern.

In this paper, results from three discharges are presented and the main parameters of the target discharges, the fast camera and the TESPEL are summarized in Table 1. The different choice of the tracer impurity for each discharge and other parameters is due to the experimental constraints. The plasma kinetic profiles are shown in Figure 3 as a function of the normalized effective radius. For discharge conditions considered in this paper, TESPEL ablation takes place in the 0.65-1 effective radius range.

It is worth discussing here that in one discharge (20180927.039) the bulk plasma species was Helium. Cryogenic pellet experiments conducted on ASDEX Upgrade tokamak have shown that the distribution of the cloud radiation is not affected by the target plasma material (studied for Hydrogen, Deuterium and Helium) [18]. This is probably explained by the fact that the cloud distribution is mainly determined by the ablation rate and by the incoming heat flux, which is predominantly transported by electrons. Based on these, we consider the results obtained in plasmas with different working gases to be comparable.

3. TESPEL cloud distribution and dynamics

In OP1.2, TESPEL was injected into numerous discharges with various magnetic configurations. More than 50 percent of the injections were recorded by the fast framing camera system, albeit with different filters and frame rates, which were changed on a shot-by-shot basis. The observation view allows us to investigate the radiation distribution of the polystyrene cloud along and perpendicular to the magnetic field lines and to determine the toroidal and vertical/poloidal movement of the cloud. Representative short exposure (H: 0.4 μ s, C: 1.9 μ s, C²⁺: 0.4 μ s) images showing H(C⁺), C and C²⁺ radiation distributions are plotted in Fig.4, using false colors. The black dashed curve is the magnetic field line crossing the TESPEL cloud, projected onto the image plane. All contour plots in this paper are normalized individually, and the same false colors (50 contours between the minimum and maximum radiation with the same color table) are used, to be able to visualize the faintly radiating drifting cloud.

As expected, the C atomic radiation has shortest extension along the magnetic field line (B_{\parallel}), while C²⁺ radiation is the most extended and has a double peaked distribution. Sometimes images made with the H α filter also have a double peaked structure which may be the consequence of the C⁺ radiation falling into the filter transmission window.

Using such snapshots, the position of the TESPEL (assuming that it coincides with the location of maximum radiation for Carbon atoms) was determined during its ablation, showing that the TESPEL follows the designated radial trajectory, *i.e.*, no toroidal and poloidal deflection was seen. For cryogenic pellets, a curved trajectory is only observed shortly before a pellet is totally ablated [21]. It is considered that with these filters only the radiation of the polystyrene shell is detected but not that of the heavy tracer impurity kernel. Therefore, the latter phase of ablation, when only the kernel is ablated and the pellet could follow a curved trajectory, is not recorded.

In order to visualize the distribution and evolution of the TESPEL cloud, intensity profiles along the magnetic field line crossing the center (black dashed line on Fig.4) of the cloud and perpendicular to the magnetic field line (B_{\perp}) at two positions (at the center, where the pellet is expected: black solid line and on the side: red solid line) were calculated. These cut lines were determined when the total radiation of the TESPEL cloud was at its maximum and were used for each image, but updated for each pellet. Figure 5 summarizes the time evolution of these intensity profiles for H(C⁺), C and C²⁺, respectively. The pixel

coordinates are converted into physical coordinates by using viewing geometry parameters and the estimated position of the TESPEL in the plasma. Due to the observation geometry we cannot calculate the pellet tracking, we only know that the pellet ablation takes place in about a 20-cm-long region located about 3 m away from the observation lens. This causes a relative error of the spatial calibration less than 3%. The B_{\perp} distributions are overplotted by the center of mass (white curves). At the bottom of Figure 5, the evolution of the total radiation detected by the camera is plotted. The vertical, colored bars represent the consecutive time instants where the radiation distributions are plotted in Figures 6, 7 and 9. The TESPEL ablation shows similar behavior than that of the cryogenic pellet: the light emission - and therefore the ablation - starts inside the confined region, it increases with time until the material of the TESPEL shell is fully consumed, then it suddenly drops to zero. The radiation and the shell lifetime lasts about 250 μs , that is, a pellet with 600 m/s travels about 15 cm in the plasma. The shift of the radiation center of mass (to negative values) in Figure 5 shows the slight mismatch between the pellet injection line and the camera viewing direction. All the radiation distributions seen in Figure 5 have a quasiperiodic behavior during the whole ablation: both the vertical position and the B_{\parallel} cloud size fluctuates with a repetition time of about 20 μs .

In order to reveal the detailed evolution of the cloud, a part of the ablation time window is zoomed in and the individual line cuts are plotted in Figures 6 and 7 for C and C^{2+} respectively. Here both the individual profiles for consecutive frames and the radiation distributions as a function of time and distance along the cut lines are plotted. It is seen here that for neutral carbon, the cloud is slightly elongated along the magnetic field line with a B_{\perp} size of about 1 cm and a B_{\parallel} size of about 1 - 2 cm (see Fig. 6). The distribution is Gaussian-like, having a single maximum. The C cloud line radiation is proportional to the product of the carbon density (which falls with distance from the pellet surface, determined by the spherical expansion of the neutral cloud) and the local target plasma electron density (the cloud electron density is low in this region - as long as the cloud is neutral) confirming the measured Gaussian-like radiation distribution.

Since cloud ions are streaming both parallel and anti-parallel to the magnetic field, the C^{2+} cloud (plasmoid) is strongly elongated along the magnetic field line with B_{\perp} size of about 1-2 cm and B_{\parallel} size of 5-20 cm. The cloud has a double-peaked structure along the magnetic field line (see Figure 7). The reason for this structure is that the C^{2+} radiation is probably dominated by electron impact excitation of cold pellet cloud electrons, which have orders of magnitude higher density than target plasma electrons (at least at cloud regions where the C^{2+} density is high). Additionally, both the C^{2+} and the cloud electron density distributions have a maximum along the magnetic field line, this being symmetric to both sides of the pellet, resulting in the double-peaked structure. These features of the neutral and ionized cloud (plasmoid) part of the TESPEL are similar to the behavior of the H pellet clouds [18].

The quasiperiodic evolution of the pellet cloud can be followed by the applied temporal resolution (525 kHz): as mentioned already, the period time is about 20 μs . For better understanding, consecutive snapshots are also plotted in Figure 8 for the last four time instances marked on Figure 7. According to Figures 7 and 8, an upward movement of the cloud starts when the ionized cloud is the widest along the field line. The cloud splits, and a part of it moves upward, leaving a small cloud around the pellet (see inset (1) and (2) of Figure 8), and detaches completely from the remaining cloud around the pellet, the latter already expanding along B_{\parallel} (inset (3) of Figure 8). Later this detached cloud disappears (it is probably further ionized and diluted) and then the cloud around the pellet becomes the dominant radiator. At the central B_{\perp} cut (black solid line) which crosses the pellet itself, a smaller movement of the radiation center of mass is observed than for the side B_{\perp} cut (red solid line). This is because close to the pellet the cloud is basically neutral and probably stays with the pellet. A smaller upward movement is also present in the neutral radiation (see Figure 6) which can be explained either by recombination of the moving ionized cloud or by drag effect.

The time window zoom for the radiation recorded by the H_{α} filter is plotted in Figure 9. The disadvantage of this experiment was that due to the width of the filter, not only hydrogen atomic radiation but also C^{+} radiation was detected. This is probably the reason why the distributions along the magnetic field line sometimes has two peaks, similarly to the C^{2+} radiation distribution. However, it is worth mentioning that H atomic radiation can also exhibit double peaked structure as seen in ASDEX Upgrade [18]. The clouds are slightly elongated along the field line and have similar dimensions like the C atom cloud. A very weak upward movement can also be observed therefore the overall behavior is very similar to that of the C cloud.

Our observations have indicated that C^{2+} radiation is the best indicator if we want to characterize the dynamics of the TESPEL cloud. This is understandable as charged particles are needed e.g. for drifting and a magnetic field aligned cloud can be well observed with the C III filter. Therefore, the position of the center of mass of C^{2+} radiation and hence its velocity (representing the drift velocity) were determined perpendicular to the magnetic field line. These quantities were calculated both along a cut line crossing the pellet and further away. The growth rate of the FWHM of the cloud parallel to the magnetic field line can account for the parallel expansion therefore this "velocity" is also calculated. All these quantities were plotted on Figure 10 together with the evolution of the total radiation and the maximum amplitude for the radiation distribution evaluated along the black and red colored solid lines in B_{\perp} direction as indicated in figure 4. It can be clearly seen here that these quantities fluctuate

and the characteristic time of fluctuation can be determined from the time difference of successive local maxima. During the ablation of one pellet several local maxima (indicated by the colored vertical arrows on Figure 10) could be identified which made it possible to determine average values. Accordingly, period times of 16 ± 2 (6) μs , 17 ± 2 (7) μs and 16 ± 2 (7) μs were obtained for parallel FWHM and for the two perpendicular cuts (mean \pm error of the mean (standard deviation)). We believe that both drift velocity and parallel propagation are best characterized by maximal velocities. However, it is worth keeping in mind that we are talking here about velocities derived from C^{2+} line radiation distributions. As the cloud particles continue to ionize, they are likely to accelerate even further, so the true velocities will probably be higher. A velocity of 8800 ± 1700 (6200) m/s was obtained for parallel expansion, while 840 ± 120 (450) m/s (crossing the pellet) 1140 ± 150 (520) m/s (side cut) for the drifts.

Finally, it is worth mentioning that the total radiation emitted by the different ionic states are also fluctuating and show some correlation with the movement of the cloud: larger movements are typically associated with local maxima of these radiation traces.

4. Discussion

The experimental results detailed in the previous section show that both the B_{\perp} and the B_{\parallel} distributions of the pellet cloud fluctuate, which is associated with a vertical cloud movement and an eruption/ejection of part of the cloud. Previous experiments with cryogenic pellets performed on W7-X have shown that the cloud formed around a pellet moves with the pellet and quasi periodically a part of this cloud detaches and drifts away [35]. In these experiments, only neutral cloud radiation could be detected, so there was no information on the movement of the ionized cloud.

From these observations, the following picture emerged for us about the evolution of the pellet cloud (see Figure 11). First the pellet cloud expands parallel to the magnetic field for about 10 μs . The neutral cloud grows slightly, while the C^{2+} cloud expands significantly, the location of the maximum radiation of the latter (C^{2+}) also moves further away from the pellet during the expansion. During this phase probably both the neutral and the ionized part of the cloud moves together with the pellet. During this time the pellet flies about 5-6 mm. When the cloud reaches a certain B_{\parallel} size, and has probably become significantly ionized, the ionized part of the cloud (plasmoid) moves vertically (typically upwards) and detaches from the pellet. This takes about an additional 10 μs . Finally, these processes are repeated. When the cloud is detached, only a considerably reduced and mainly neutral cloud remains around the pellet. It is worth mentioning, that because of the view geometry, the radial movements cannot be observed, therefore we cannot reconstruct the whole 3D evolution. However, we expect a strong radial (outward) drift of the pellet cloud, too. In tokamaks (ASDEX Upgrade) a similar vertical movement of the detaching pellet cloud was observed during radial $\text{grad}(B)$ drift for H pellets as well [21]. However, it is worth noting that the observed vertical movement of the detaching pellet cloud might be qualitatively in line with expectations for the pellet injection cases in W7-X that are described in this paper, while the physical process that causes the vertical movement that has been observed in ASDEX Upgrade has not yet been ascertained.

One possible reason for the upward movement of the detached cloud is the magnetic geometry. For standard magnetic configuration the radial and vertical component of $\text{grad}(B)$ is plotted on Figure 12 at the toroidal angle of the TESPEL injection. Beside a strong radial component which may be responsible for radial outward drift of the pellet cloud a clear vertical component is present. Figure 13 shows these two components and their projection to the normal direction of the line of sight of the camera observation along the TESPEL injection line. Due to the fact that the viewing direction makes a small angle with the horizontal direction, the vertical gradient contributes more to the upward-looking cloud displacement than the radial component, at least on the outer half of the plasma. Therefore, we can say that the vertical gradient may cause the upward movement of the cloud. However, considering the projection of the radial direction to our camera view, we can conclude that the radial gradient can contribute an additional 50% to the observed upward movement of the pellet cloud. This gradient can polarize the pellet cloud and form an electric field which through $E \times B$ drift moves the pellet cloud upward. This $\text{grad}(B)$ caused drift is independent of the magnetic field direction which is in agreement with our finding: typically, upward drift was observed for reversed field as well.

The measured drift speed compares well with simple theoretical predictions. Relevant papers [36,37,38] describe the acceleration of the pellet cloud (plasmoid) as follows:

$$\frac{dv}{dt} = \frac{2(p_0 - p) \nabla B}{n_0 m_i B}$$

where p_0 and p are the pressure of the plasmoid and the ambient plasma, respectively, n_0 is the particle density of the plasmoid and m_i is the ion mass of the plasmoid material. Considering that $p_0 \gg p$, and expressing p_0 as a function of n_0 and T_0 we get:

$$\frac{dv}{dt} = \frac{2k_B T_0}{m_i} \frac{\nabla B}{B}$$

Taking $T_0 = 10$ eV, $\nabla B = 0.5$ T/m, $B = 2.5$ T and a plasmoid lifetime of 10 microsecond, we get a maximum radial drift speed of 4 km/s for pure H ions, 320 m/s for pure C ions and 600 m/s for a mixture of H and C ions by using the average particle mass of the two ion species.

The explanation is also supported by HPI2 simulations [36] which can handle this problem in a much more complex and realistic way. The full magnetic geometry of W7-X is included in this code, which was slightly modified to model the TESPEL cloud drift. The polystyrene sublimation energy and an average ion mass in the calculation of the ablation and evolution of the cloud was used. This is a bit rough approximation, but it should be enough to estimate the order of magnitude of the vertical drift. Considering the standard magnetic configuration and typical target plasma electron density and temperature profiles the code calculated the evolution of the cloud drift velocity at different magnetic surfaces along the TESPEL trajectory in addition to the pellet cloud parameters. The result of the calculation shows, that an upward drift velocity is developed in a few tens of microsecond. Its maximum value was in the order of 1000 m/s, which is in line with the velocity estimated from the experimental data. The evolution of the simulated drift velocity is slower than the experimental one which can be explained by the long toroidal range of the averaging in the code which leads to a lower cloud pressure close to the TESPEL surface.

Note that the magnetic field also has a radial gradient (see Figure 12), which can lead to a radial cloud drift pointing outward. The present observation geometry did not permit investigating the cloud drift in the radial direction, but a new vertical observation line is under development to perform such experiments in the next W7-X experimental campaign, so that at least we can reconstruct the 3D evolution of the C^{2+} cloud. Furthermore, this new view allows the pellet to be tracked during ablation and therefore we can also determine the target plasma parameters along the pellet trajectory, which will allow to study the dependence of the drift parameters (velocity, periodicity) on plasma parameters (e.g. temperature).

Acknowledgements

This work has been carried out within the framework of the EUROfusion Consortium and has received funding from the Euratom research and training programme 2014-2018 and 2019-2020 under grant agreement No 633053. The views and opinions expressed herein do not necessarily reflect those of the European Commission.

One of the authors (N.T.) acknowledges financial supports from the JSPS KAKENHI 17KK0121, the NIFS/NINS Program for Enhancing Research Collaboration (UFEX105), the NIFS/NINS Young Researchers Supporting Program (UFEX106), the NIFS/NINS under Strategic International Research Exchange Promotion Program (UFEX402), and the NINS program of Promoting Research by Networking among Institutions (Grant No.01411702).

K.J.M. acknowledges support from MICINN (FIS2017-89326R).

References

- [1] Lang P T et al 2018 *Nuclear Fusion* **58** 036001
- [2] Baldzuhn J et al 2019 *Plasma Phys. Control. Fusion* **61** 095012
- [3] Baldzuhn J et al 2018 *Plasma Phys. Control. Fusion* **60** 035006
- [4] Müller H W et al 2002 *Nuclear Fusion* **42** 301
- [5] Lang P T et al 1997 *Phys. Rev. Letters* **79** 1487
- [6] Lang P T et al 2004 *Nuclear Fusion* **44** 665
- [7] Baylor L R et al 2013 *Phys. Rev. Letters* **110** 245001
- [8] Herfindal J L et al 2019 *Nuclear Fusion* **59** 106034
- [9] Goncharov P R et al 2006 *Fusion Sci. and Technol.* **50** 222
- [10] Fisher R K et al 1995 *Phys. Rev. Letters* **75** 846
- [11] Kocsis G et al 1999 *Plasma Phys. Control. Fusion* **41** 881
- [12] Ledl L et al 2004 *Nuclear Fusion* **44** 600
- [13] Bortolon A et al 2019 *Nuclear Fusion* **59** 084003
- [14] Pégourié B 2007 *Plasma Phys. Control. Fusion* **41** R87
- [15] Lengyel L L et al 1999 *Nuclear Fusion* **39** 791
- [16] Sergeev V. Yu. et al 2006 *Plasma Phys. Reports* **32** 363
- [17] Parks P B et al 1978 *Phys. Fluid* **21** 1735
- [18] Cseh G et al 2017 *Nuclear Fusion* **57** 016022
- [19] Rozhansky V et al 2004 *Plasma Phys. Control. Fusion* **46** 575

-
- [20] Müller H W et al 1999 *Phys. Rev. Letters* **83** 2199
 [21] Kocsis G et al 2004 *Rev. Sci. Instrum.* **75** 4754
 [22] Baldzuhn J et al 2004 *Plasma Phys. Control. Fusion* **35** 1413
 [23] Sudo S et al 2012 *Rev. Sci. Instrum.* **83** 023503
 [24] McCarthy K J et al 2017 *EPL* **120** 25001
 [25] Sharov I A et al 2018 *PTech. Physics Letters* **44** 384
 [26] Sharov I A et al 2015 *Rev. Sci. Instrum.* **86** 043505
 [27] Bosch H S et al 2017 *Nuclear Fusion* **57** 116015
 [28] Wolf R C et al 2016 *IEEE Trans Plasma Sci.* **44** 1466
 [29] Klinger T et al 2017 *Plasma Phys. Control.* **59** 014018
 [30] Wolf R C et al 2017 *Nuclear Fusion* **57** 102020
 [31] Klinger T et al 2019 *Nuclear Fusion* **59** 112004
 [32] Sunn Pedersen T et al 2019 *Nuclear Fusion* **59** 096014
 [33] Sudo S et al 2013 *Plasma Phys. Control. Fusion* **55** 095014
 [34] Bussiahn R et al 2018 *Rev. Sci. Instrum.* **89** 10K112
 [35] G. Kocsis et al 2018 ECA Vol. 42A, P4.1066
 [36] N. Panadero et al 2018 *Nucl. Fusion* **58** 026025
 [37] B. Pégourié et al 2007 *Nucl. Fusion* **47** 44
 [38] A. Matsuyama et al 2012 *Nucl. Fusion* **52** 123017
 [39] A.R. Polevoi et al 2017 *Nucl. Fusion* **57** 022014
 [40] A.R. Polevoi et al 2018 *Nucl. Fusion* **58** 056020

Discharge number	20180919 024	20180927 039	20180906 025
Bulk plasma species	H	He	H
Magnetic configuration	Standard	Standard	Standard
Heating power	4 MW	4 MW	6 MW
W_{DIA}	500 kJ	480 kJ	630 kJ
Cam. frame rate	372 kHz	525 kHz	525 kHz
Camera exposure time	0.4 μ s	1.9 μ s	0.4 μ s
Filter	H (C ⁺)	C	C ²⁺
TESPEL speed	580 m/s	470 m/s	580 m/s
TESPEL shell outer diameter & thickness	0.9 mm/ 0.32 mm	0.7 mm/ 0.22 mm	0.9 mm/ 0.32 mm
Tracer material	Si/Cu	Fe	Cu

Table 1 Target plasma, camera and TESPEL parameters for the presented discharges.

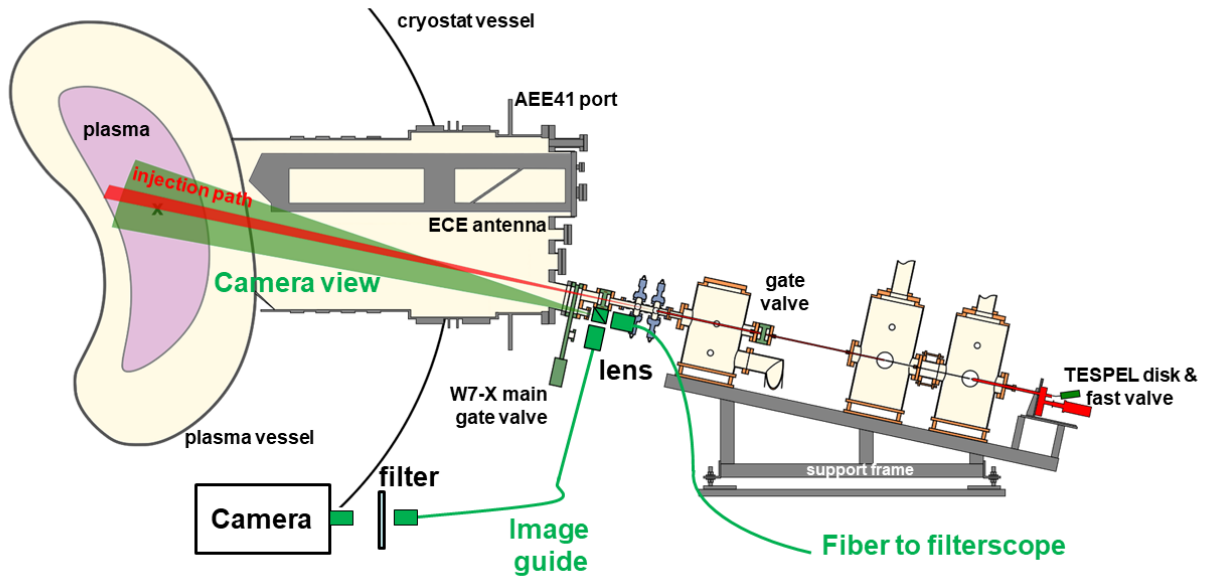


Figure 1 Sketch of the poloidal cross section of the TESPEL injection. The TESPEL injector and the diagnostics are also depicted. The red cone represents the estimated TESPEL injection cone (which is inclined at about 12° relative to the horizontal direction) and the green cone the view of the fast camera. The image is transferred to the camera by a wound fiber bundle (image guide). The interference filter is installed within the relay optics (two opposite commercial camera lenses).

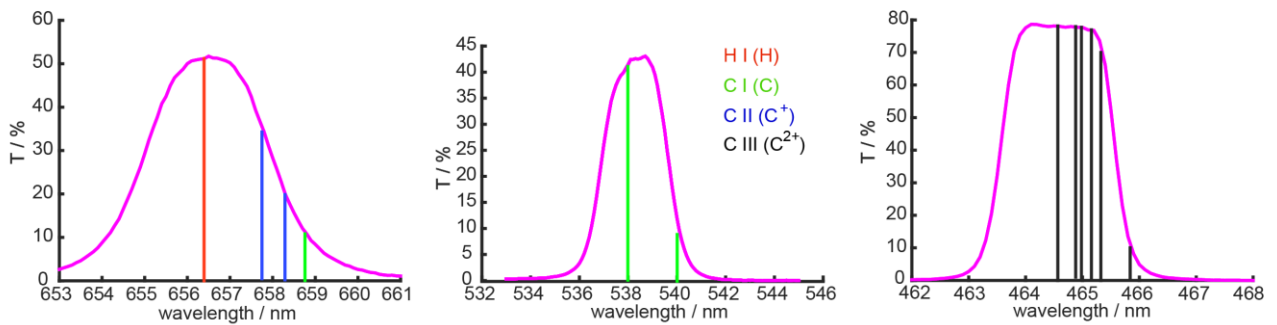


Figure 2 Measured transmission curves of the applied interference filters and selected intensive lines of the first three ionisation states of Carbon and H α radiation.

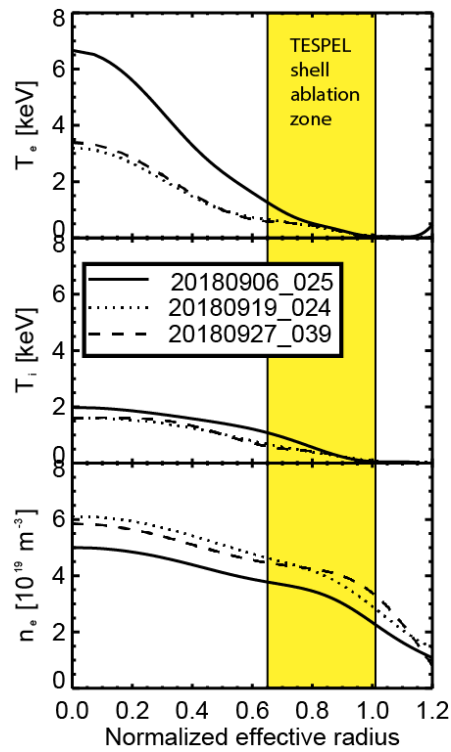


Figure 3 The plasma kinetic profiles as a function of the normalized effective radius. For these discharges TESPEL ablation takes place in the 0.65-1 effective radius range.

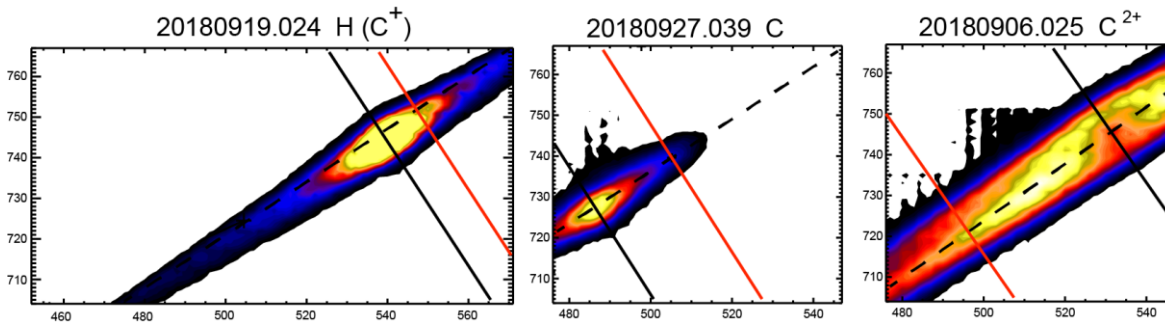


Figure 4 Typical snapshots recorded with the applied three interference filters. In order to visualize the distribution and evolution of the TESPEL cloud, intensity profiles along the magnetic field line crossing the center (black dashed line) of the cloud and perpendicular to the magnetic field line (B_{\perp}) at two positions (at the center, where probably the pellet is located: black solid line and further away: red solid line) were calculated.

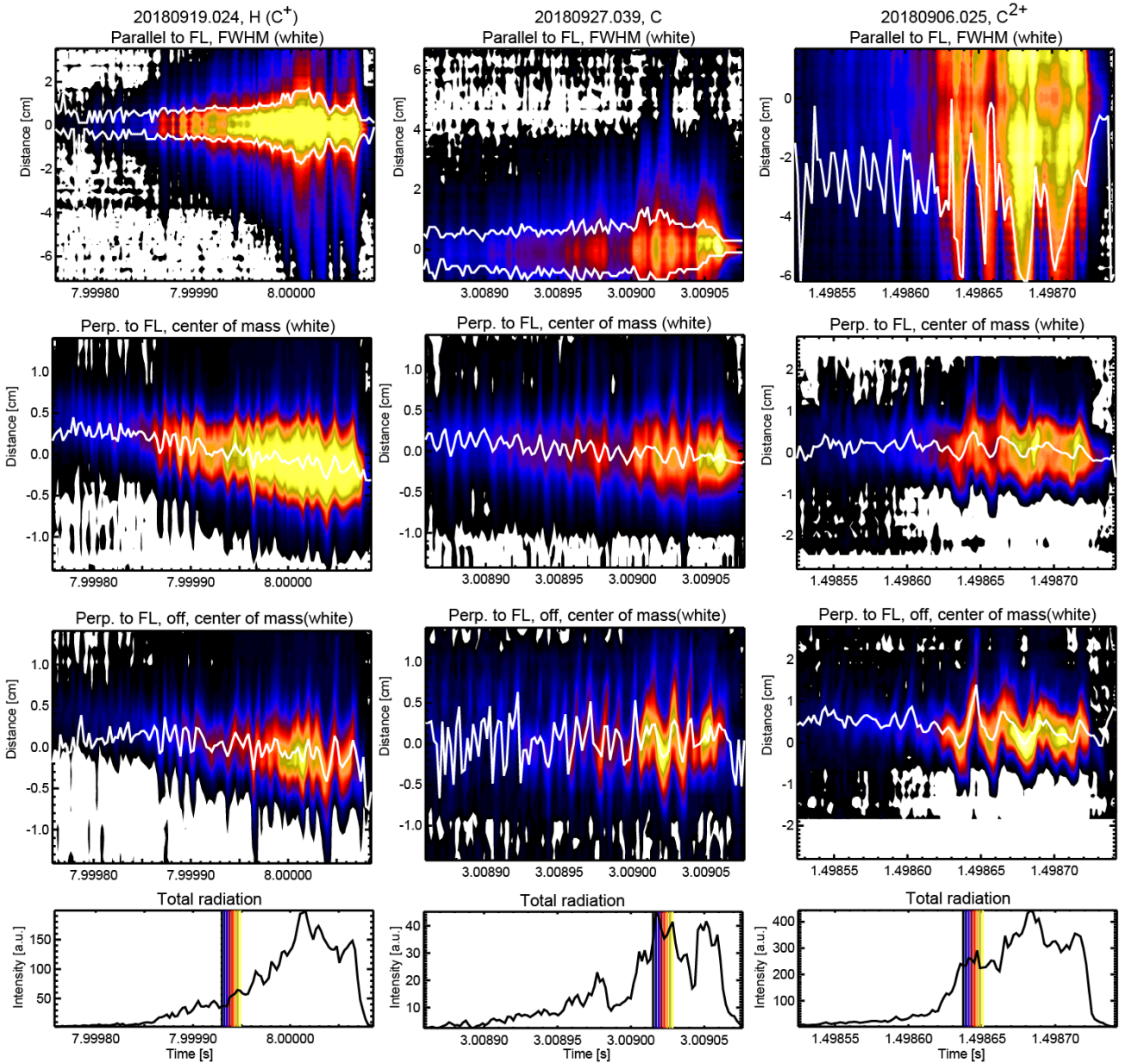


Figure 5 Intensity profiles along the selected lines (for definition see Fig. 4) as a function of time during the TESPEL ablation as contour plots for H α (left column), C (middle column) and C $^{2+}$ (right column) radiation. These three cases are recorded in separate plasma discharges. The figures from top to bottom are the radiation distributions parallel (dashed line on Fig. 4) and perpendicular (solid line on Fig. 4) to the field line crossing the cloud center and perpendicular but crossing the cloud edge (red solid line on Fig. 4). The white curves show FWHM of the parallel distribution and the radiation center of mass of the perpendicular distributions. The lowest figures represent the total radiation recorded by the camera; the overplotted vertical lines represent the times of eight consecutive light distributions plotted on Fig. 6, 7 and 9.

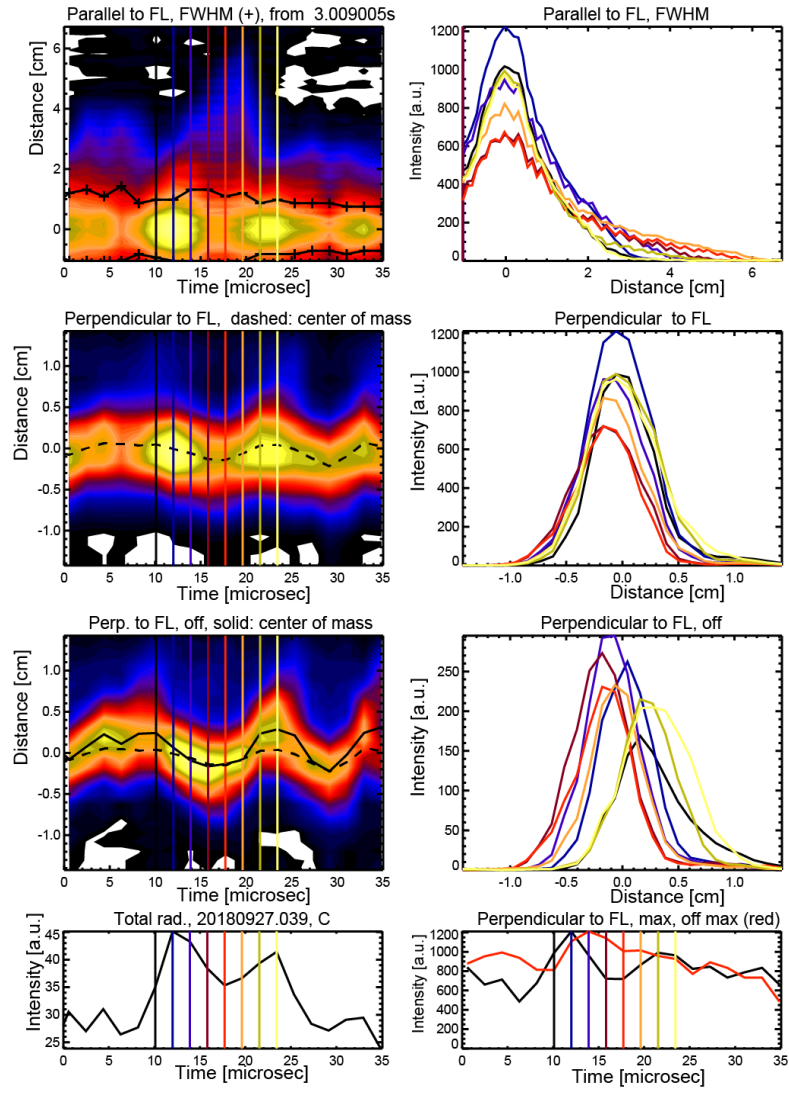


Figure 6 Time window zoom of the contour plots for C radiation distributions (left figures) and individual intensity distributions cut from eight consecutive images (right figures). For cuts along the field line the FWHM are also over plotted (upper left figure); for the perpendicular cuts the radiation center of mass (dashed curve for the cut crossing the cloud center, solid curve cut on the side). Bottom left: total radiation, bottom right: maximum amplitude as function of time for the radiation distribution evaluated along the black and red colored solid lines in B_{\perp} direction as indicated in Figure 4.

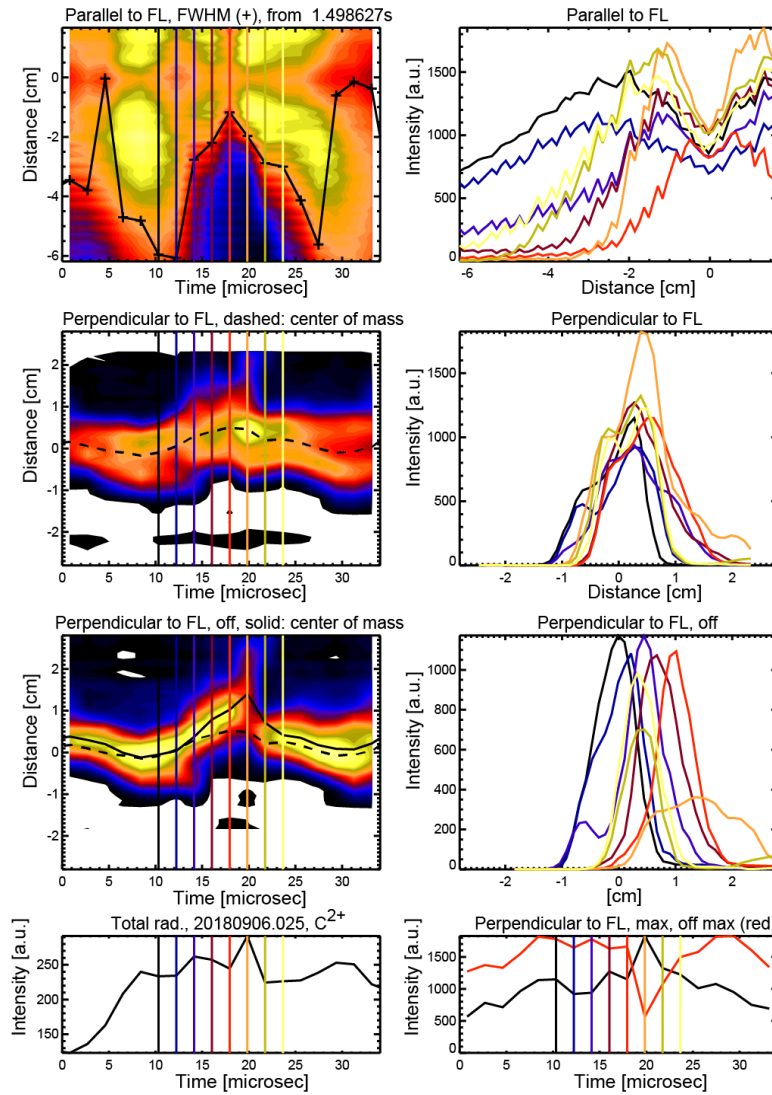


Figure 7 Time window zoom of the contour plots for C^{2+} radiation distributions (left figures) and individual intensity distributions cut from eight consecutive images (right figures). For further details, see Fig.6.

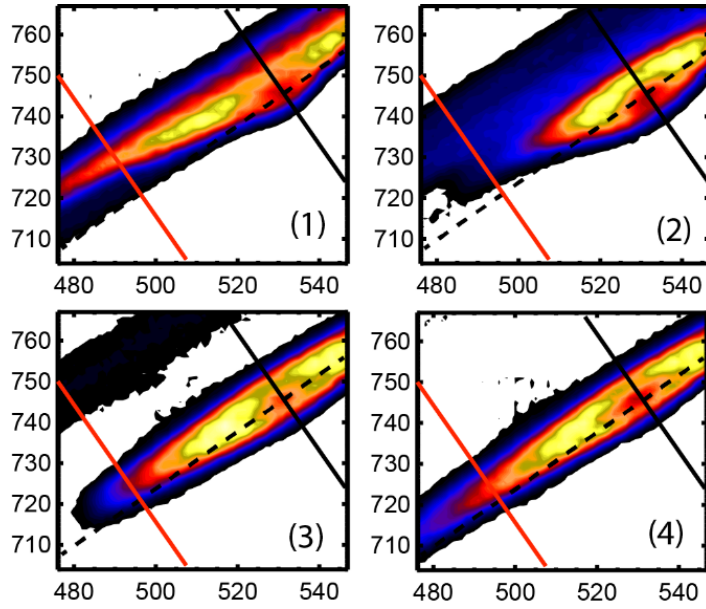


Figure 8 Consecutive snapshots made with C^{2+} filter. The pellet is roughly at the crossing of the black solid and dashed lines. The intensity cuts of the plotted lines are seen on Fig.7 (last four selected time instances).

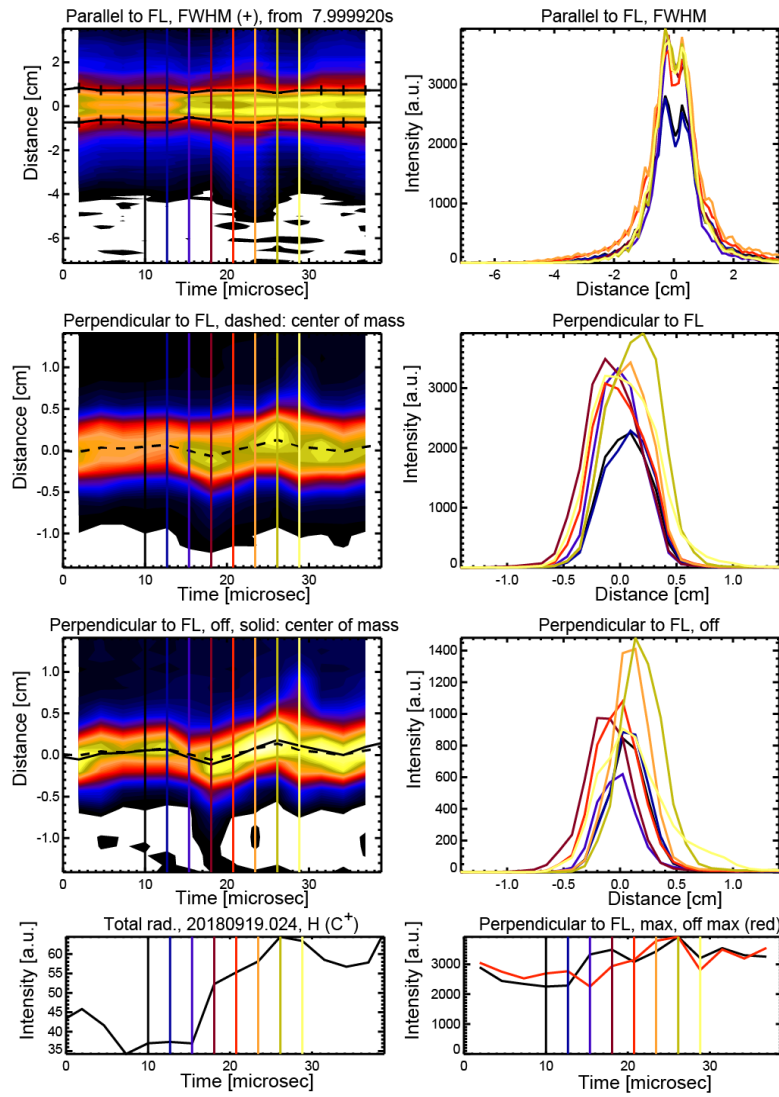


Figure 9 Time window zoom of the contour plots for H α radiation distributions (left figures) and individual intensity distributions cut from eight consecutive images (right figures). For further details, see Fig.6.

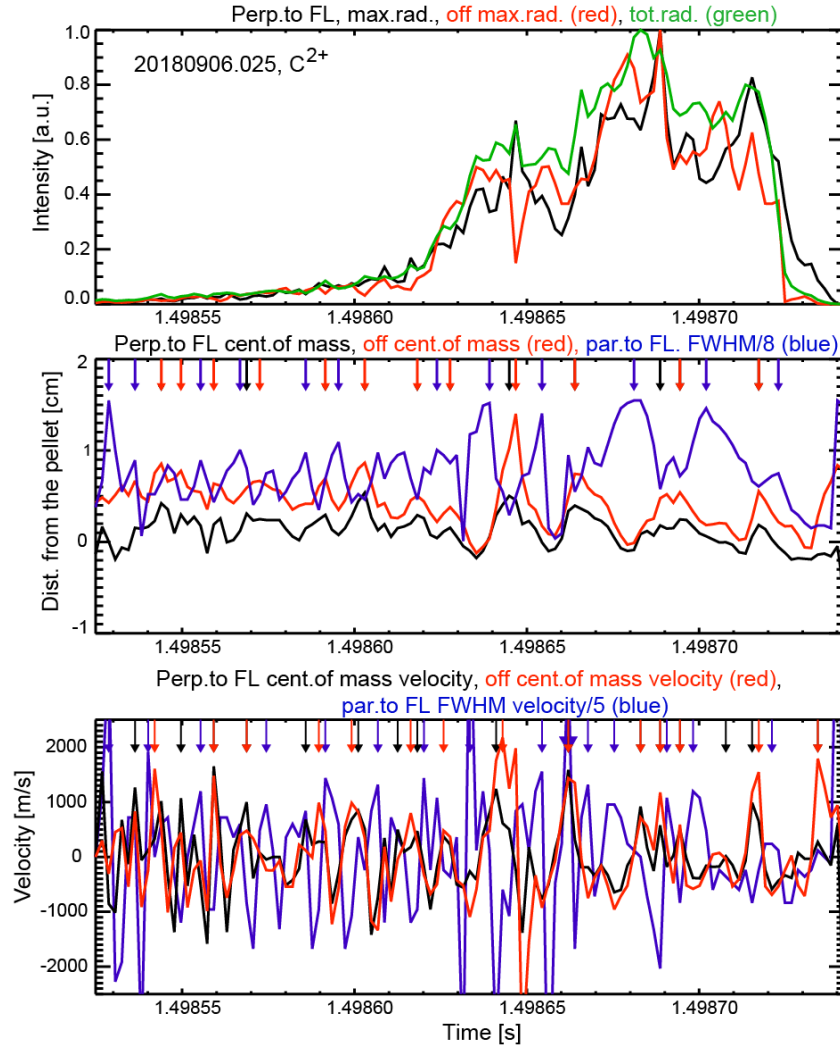


Figure 10. The evolution of the total radiation (green) and the maximum amplitude for the radiation distribution evaluated along the black and red colored solid lines in B^\perp direction as indicated in Figure 4 (upper plot). On the middle the position of the center of mass of C²⁺ radiation distribution evaluated along the black and red colored solid lines in B^\perp direction as indicated in Figure 4 and FWHM/8 of the radiation distribution along magnetic field line crossing the pellet (blue) are plotted as function of time. The determined local maxima of this quantities are also overplotted by vertical arrows (same color). The propagation velocity of these three quantities and their local maxima (vertical arrows) are plotted on the lower plot.

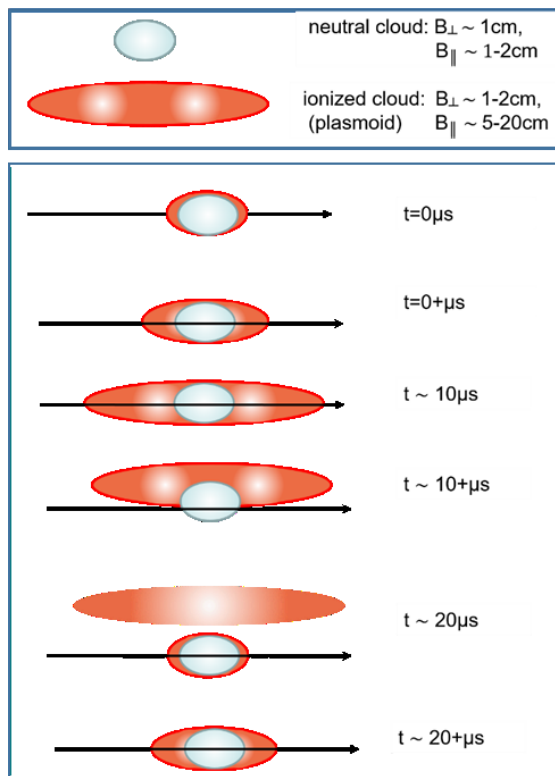


Figure 11 Cartoon of the TESPEL cloud evolution. The blueish ellipsoid represents the neutral cloud, the reddish the ionized cloud (plasmoid).

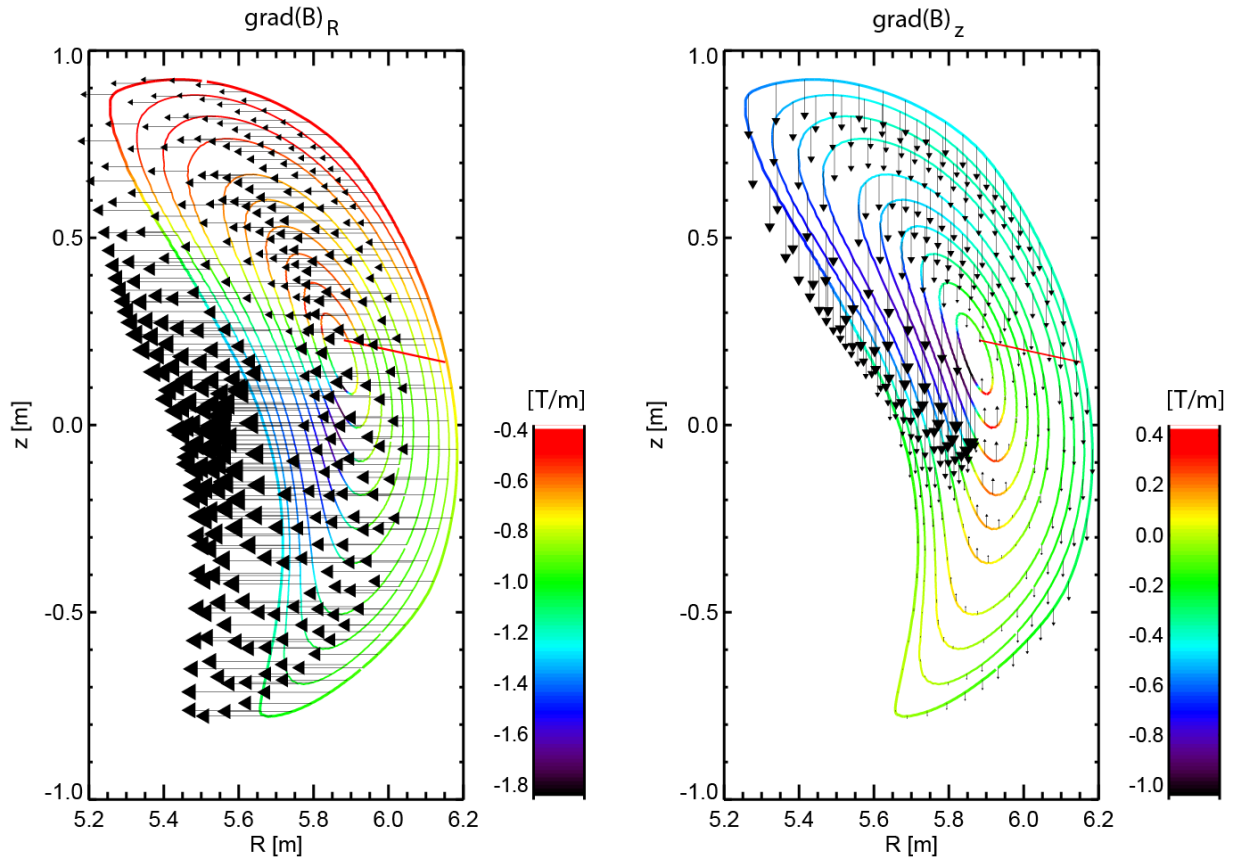


Figure 12 Magnetic surfaces of the standard configuration at the toroidal angle of the TESPEL injection. The red solid line represents the TESPEL injection line. The color code and the black arrows show the magnitude of the radial (left) and the vertical (right) component of the $\text{grad}(B)$.

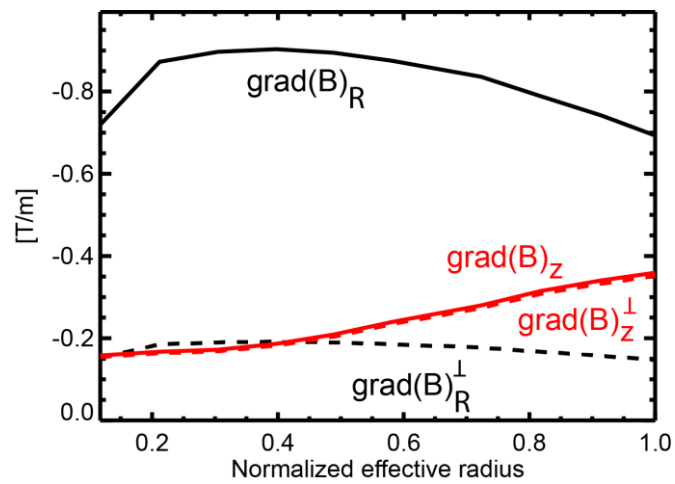


Figure 13 The radial (black solid line) and the vertical (red solid line) component on the $\text{grad}(B)$ along the TESPEL injection line as a function of the normalized effective radius. The dashed lines represent these components projected to the normal of the line of sight of the observation.